Noninvasive two-photon microscopy imaging of mouse retina and retinal pigment epithelium through the pupil of the eye

Grazyna Palczewska[1], Zhiqian Dong[1], Marcin Golczak[2], Jennifer J Hunter[3–5], David R Williams[3,6], Nathan S Alexander[2] & Krzysztof Palczewski[1,2]

Two-photon excitation microscopy can image retinal molecular processes *in vivo*. Intrinsically fluorescent retinyl esters in subcellular structures called retinosomes are an integral part of the visual chromophore regeneration pathway. Fluorescent condensation products of all-*trans*-retinal accumulate in the eye with age and are also associated with age-related macular degeneration (AMD). Here, we report repetitive, dynamic imaging of these compounds in live mice through the pupil of the eye. By leveraging advanced adaptive optics, we developed a data acquisition algorithm that permitted the identification of retinosomes and condensation products in the retinal pigment epithelium by their characteristic localization, spectral properties and absence in genetically modified or drug-treated mice. This imaging approach has the potential to detect early molecular changes in retinoid metabolism that trigger light- and AMD-induced retinal defects and to assess the effectiveness of treatments for these conditions.

Noninvasive imaging of biochemical processes at subcellular resolution *in vivo* represents a new frontier in discovering the details of biological processes and the impact of disease and therapies. Two-photon excitation microscopy (TPM) based on two-photon excitation (2PE) fluorescence imaging can further these discoveries by use of infrared excitation light that nondestructively penetrates deep into tissues[1].

2PE is well suited for retinal imaging because the sclera, cornea and lens are highly transparent to infrared light[2–5]. The 2PE rate is proportional to the square of incident light intensity[6]. Therefore, using adaptive optics to correct for wavefront errors introduced by the lens and cornea[7–10] improves resolution and maximizes the 2PE rate[11] by achieving a tightly focused excitation beam. However, the two-photon absorption cross-sections of native fluorophores are small (on the order of 1×10^{-52} cm^4 s per photon)[12], which necessitates improvements in 2PE imaging efficiency. The number of photons generated by 2PE is inversely proportional to the laser pulse duration[6], and therefore application of lasers delivering pulses shorter than 75 fs, coupled with correction for group delay dispersion, can more than double 2PE-induced fluorescence[13]. Further improvements come from highly sensitive low noise detectors with thermoelectric cooling and from the application of sophisticated software algorithms for image acquisition and analysis. With these advances, biochemical processes in the retinal pigment epithelium (RPE) and the neuronal cells can be monitored[5].

The fluorophore content of the retina-RPE region reflects the efficiency of the visual cycle (i.e., visual chromophore 11-*cis*-retinal regeneration) and changes in response to external stress, genetic manipulations and treatments[14–16]. Retinoids are intrinsic fluorophores with absorption spectra that respond to 2PE (refs. 3,4). During aging, retinal retinoids form condensation products, such as di-retinoid-pyridinium-ethanolamine (A2E), that are fluorescent[17] and detectable by TPM and serve as biomarkers for potentially toxic retinoids that form early in degenerative retinopathies such as Stargardt's disease and AMD[5,18].

The challenge now is to develop TPM instrumentation[7] that can safely and periodically image the retina and RPE to detect and follow abnormalities in biochemical transformations well before electrophysiological and pathological changes become evident. Here, we present a major step toward this goal.

RESULTS

RPE imaging through a mouse eye pupil

To image the RPE and retina in live mice, we assembled an instrument containing a 75-fs laser with integrated group delay dispersion precompensation, adaptive optics modulating the excitation light and a fluorescence detector in a nondescanned configuration (**Fig. 1a**). We obtained initial images of RPE created by endogenous fluorophores with *ex vivo* mouse eyes submerged in PBS and a deformable mirror (DM) set to a neutral position (**Fig. 1 a–c**). We optimized dispersion precompensation, which increased the mean fluorescence an average of fivefold (**Fig. 1d**), indicating that in the RPE, 75-fs laser pulses would elongate to 400 fs (ref. 6). Iterative changes of the DM surface shape (**Fig. 1e**) resulted in further increased mean fluorescence, from 34.6 to 58.1 in arbitrary units, and increased the dynamic range of

[1]Polgenix, Cleveland, Ohio, USA. [2]Department of Pharmacology, Case Western Reserve University, Cleveland, Ohio, USA. [3]Center for Visual Science, University of Rochester, Rochester, New York, USA. [4]Flaum Eye Institute, University of Rochester, Rochester, New York, USA. [5]Department of Biomedical Engineering, University of Rochester, Rochester, New York, USA. [6]The Institute of Optics, University of Rochester, Rochester, New York, USA. Correspondence should be addressed to K.P. (kxp65@case.edu).

Figure 1 TPM for imaging of mouse retina and RPE. (**a**) TPM system layout. DC, group velocity dispersion precompensation; EOM, electro-optic modulator; DM6000, upright microscope; PMT, photomultiplier tube. (**b**) Dichroic mirror (DCh) and barrier filter 680 SPET separate fluorescence and excitation light. NA, numerical aperture. (**c**) Layout of the adaptive optics system. FMK1 and FMK2, fold mirrors on kinematic magnetic bases; L1, L2, L3 and L4, lenses; FM1, FM2 and FM3, fold mirrors. (**d**) Left, images of *ex vivo* RPE from a 1-month-old *Abca4*^{−/−}; *Rdh8*^{−/−} mouse after exposure to bright light, obtained with (top) and without (bottom) DC. Right, mean fluorescence measured with and without DC; error bars indicate mean ± s.d., *n* = 3 eyes. (**e**) Top row, images of *ex vivo* RPE from a 3-month-old *Rpe65*^{−/−} mouse obtained during DM optimization; left to right, the start of optimization with DM in the neutral position to completion of the imaging session. Trial, image obtained with nonoptimal DM settings; optimal, image obtained with DM settings that improved image quality. Bottom row shows the corresponding DM surfaces. (**f**) Quantification of image quality from **e**. m, mean. Scale bars, 100 μm (**d** and **e**).
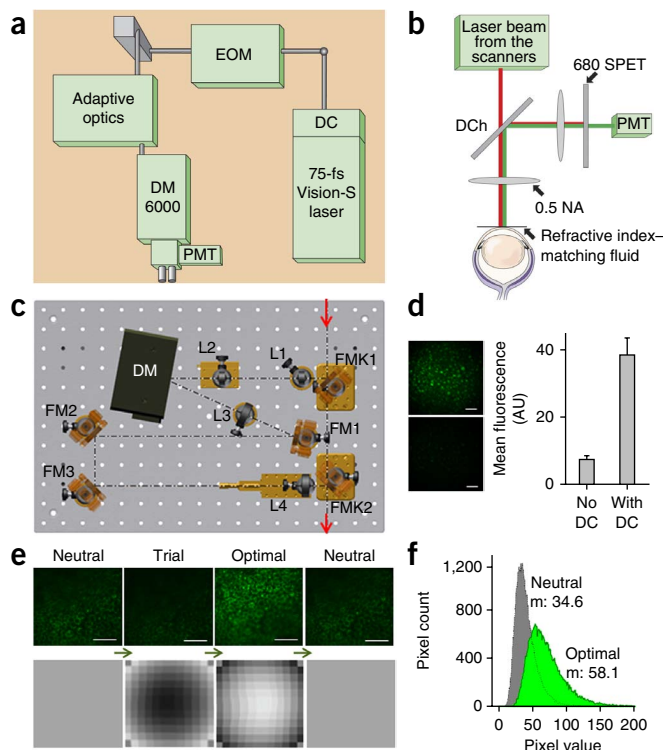
images, quantified as the range of pixel values from 176 to 237, with 255 being the maximum (**Fig. 1f**).

To assess the capabilities of our system to characterize the RPE and retina, we imaged *ex vivo* eyes of albino mice with different genetic backgrounds. We obtained the brightest RPE images in *Rpe65*^{−/−} mice in response to 730-nm excitation (**Fig. 2a**). The brightly fluorescent granules correspond to enlarged retinosomes, which are a characteristic feature of the RPE only in *Rpe65*^{−/−} mice owing to blockade of 11-*cis*-retinol synthesis[3,5,19]. Double nuclei and retinosomes located close to individual cell membranes were also resolved (**Fig. 2a**). In contrast to those in *Rpe65*^{−/−} mice, predominant fluorophores in the RPE of *Abca4*^{−/−}; *Rdh8*^{−/−} (DKO) mice were retinal condensation products[5], a result of impaired clearance of all-*trans*-retinal upon its liberation from activated rhodopsin. Imaging these mice allowed us to show the ability of TPM to detect retinal condensation products. Fluorophores in these mice were more visible with an 850-nm excitation and were uniformly distributed within RPE cells; consequently, the black nuclei, free of fluorophores, were defined in TPM images (**Fig. 2b**). Retinosomes were visible in wild-type (WT) B6(Cg)-Tyr[c-2J]/J mice

exposed to white light for 30 min at 5,000 lx before imaging (**Fig. 2c**) and were more clearly visible in WT mice pretreated with retinylamine (Ret-NH$_2$), a powerful inhibitor of the retinoid cycle[20], even though we reduced the laser power by 17% for the same detector settings (**Supplementary Fig. 1**). We also imaged and counted the neuronal nuclei in the ganglion cell layer at 0.6 mm eccentricity and found 2,500 nuclei per mm^2 (**Fig. 2d**), which is fewer than the previously reported ~7,000 per mm^2 of combined ganglion and displaced amacrine cells[21] in stained retina. This difference can be explained by a combination of factors: (i) nuclei are free of fluorophores and are only visible as dark structures against brighter cell bodies, which can lead to obstruction of the nuclei by axon bundles[22,23]; (ii) not all the cell nuclei were at the same imaging depth; and (iii) the estimates of the area could be off by 40% because they were determined by comparing measurements of optic disks in *en face* TPM images to histological sections. Considering that not all the cell nuclei were at the same location along the optical axis[24], the difference by only half of a ganglion cell soma diameter would place some of the somas out of TPM focus because (i) the range of retinal ganglion cells somas diameters is 7–30 μm (ref. 25); (ii) the theoretical optical resolution along the optical axis, estimated as described by Zipffel *et al.*[26], was ~4.5 μm; and (iii) different layers of the retina come in and out of focus (**Supplementary Video 1**). Despite variances in absolute values of ganglion cell density, TPM-based visualization provides a noninvasive method for verification of the health of ganglion cell layer[10].
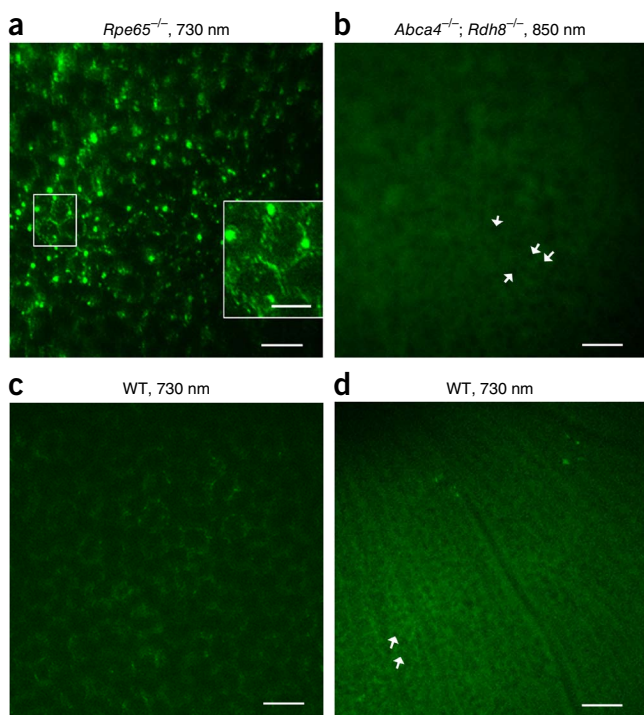
Figure 2 TPM images of *ex vivo* albino mouse RPE and retinas obtained through the mouse eye pupil. (**a**) The RPE in a 3-month-old *Rpe65*^{−/−} mouse eye. The inset in the right bottom quarter provides a magnified view of the RPE from the area outlined with a white rectangle. (**b**) The RPE in 6-month-old *Abca4*^{−/−}; *Rdh8*^{−/−} mouse eye. (**c**) The RPE in 2-month-old WT mouse eye. (**d**) The ganglion cell layer in 2-month-old WT mouse eye. White arrows in **b** and **d** point to the nuclei. Scale bars, 50 μm (all images except inset in **a**); inset scale bar, 30 μm. Excitation wavelengths and genetic backgrounds are listed in each image.

Figure 3 Use of TPM imaging for ophthalmic drug screening. (**a**) Visualization of the impact of treatment with Ret-NH$_2$ on bright light–induced accumulation of fluorescent granules in a 1-month-old $Abca4^{-/-}$; $Rdh8^{-/-}$ mouse. Representative *ex vivo* images obtained 7 and 14 d after bright light exposure; images obtained with a 'through the sclera' configuration are included for comparison. Top row, excitation with 730 nm; bottom row, excitation with 850 nm. (**b**) Individual rod photoreceptors expressing rhodopsin-GFP fusion protein in the photoreceptor layer of the retina from a 2-month-old Rho^{tm2Jhw} mouse. (**c**) 2PE emission spectra from fluorescent granules in the RPE of an $Abca4^{-/-}$; $Rdh8^{-/-}$ mouse obtained through the sclera (black) and pupil (red). Spectrum from photoreceptors in a Rho^{tm2Jhw} mouse is shown in gray. (**d**) Quantification of Ret-NH$_2$ impact on accumulation of fluorescent granules in the RPE, based on images shown in **a**; ND, none detected. Error bars indicate mean ± s.d., $n = 3$ eyes per group. (**e**) Lower zoom image of the RPE in a 6-week-old mouse not treated with Ret-NH$_2$, with the optic disc shown in the top image. Bottom image shows a magnified view from the RPE area outlined with white rectangle in the top image. Scale bars, 30 μm (**a**, **b** and bottom image of **e**) and 220 μm (top image of **e**).
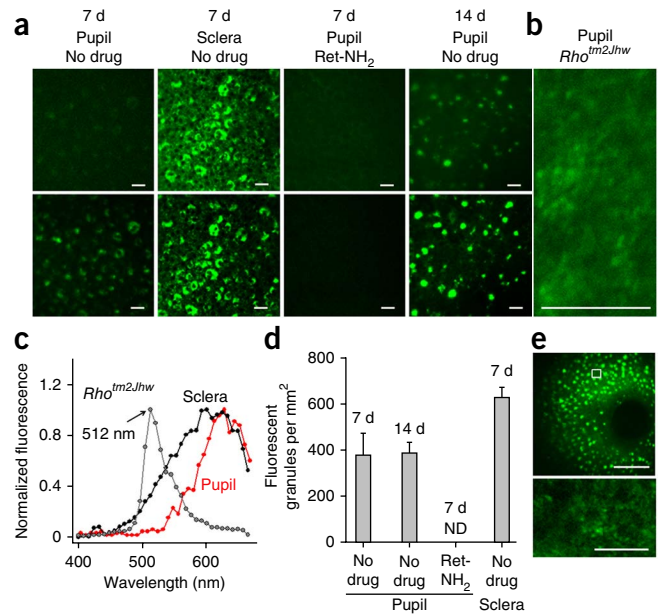
Evaluation of drug therapy on RPE preservation

It has been previously shown that Ret-NH$_2$ protects mouse RPE and retina from deterioration caused by prolonged exposure to bright light[18]. Using 2PE transpupil imaging *ex vivo* at 7 and 14 d after bright light exposure, we found an overaccumulation of fluorescent granules in the RPE of untreated control DKO mice but no deposits in DKO mice treated with Ret-NH$_2$ (**Fig. 3a**). These granules were more clearly visible when imaged with 850-nm rather than 730-nm light, indicating that they were condensation products of all-*trans*-retinal. Before we measured their emission spectra, as a control for measurements of spectra, we performed transpupil imaging of the retina of Rho^{tm2Jhw} mice expressing rhodopsin-GFP fusion in the photoreceptor outer segments[27] (**Fig. 3b**) and determined that the emission maximum from photoreceptors of these mice was at 512 nm (ref. 27). The maximum and the spectra were almost identical to

those obtained through the sclera (**Supplementary Fig. 2**) and the maximum was almost identical to the previously published maximum at 511 nm (ref. 28). The emission spectra from granules in DKO mice had maximum at 628 nm. Even though slightly red-shifted, these spectra are comparable with those observed in previous reports[17], which confirms granule origin as all-*trans*-retinal condensation products (**Fig. 3c**). Emission spectra obtained through the sclera showed a higher contribution of fluorophores emitting at shorter wavelengths (**Fig. 3a**) than the spectra obtained with transpupil imaging, and this difference was possibly caused by spectral filtering introduced by the retina or anterior optics.

Counts of the fluorescent granules revealed no differences in the quantity of these granules at 7 d and 14 d after bleaching (**Fig. 3d**). Double nuclei and RPE cell borders are visible in the bottom image of **Figure 3e**.

Localization of bright fluorescent granules

Using a *z*-axis translation stage in our *in vivo* imaging system (**Fig. 4a**), we determined that the fluorescent granules responding to 850-nm excitation in live pigmented DKO mice exposed to bright light were located 3.0 mm away from the cornea (**Fig. 4b**). With 730-nm excitation, we imaged retinosomes in live albino $Rpe65^{-/-}$ mice 3.2 mm posterior to the cornea; differences probably resulted from mouse-to-mouse random variations[29]. We observed no fluorescence in these mice using 850-nm light[5,30] (**Fig. 4c**). We obtained the spectrum from
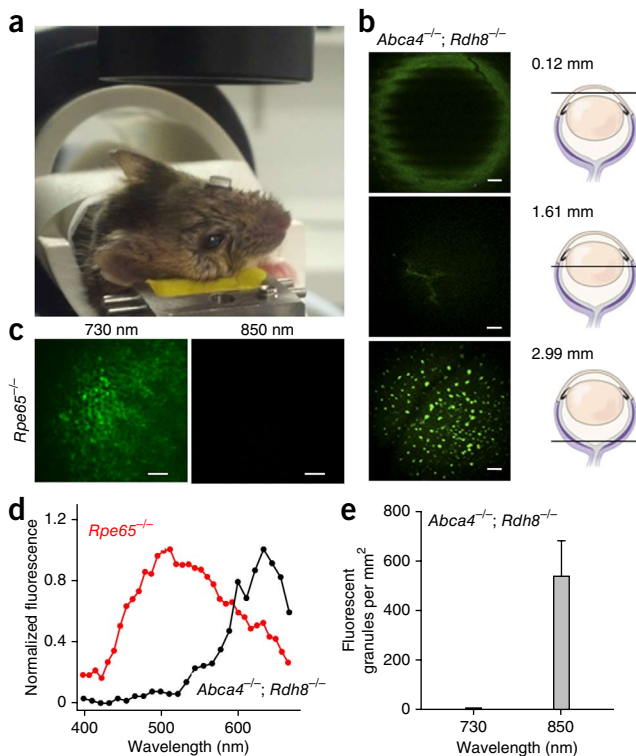

Figure 4 Setup for TPM RPE imaging in living mice. (**a**) During imaging, a contact lens covers the mouse eye facing the objective. (**b**) Representative images of a pigmented 7-week-old $Abca4^{-/-}$; $Rdh8^{-/-}$ mouse eye obtained *in vivo* with 850-nm excitation 14 d after exposure to bright light, at different depths along the *z* axis: a 120-μm section through the cornea (top), a 1,608-μm section showing lens sutures (middle) and a 2,987-μm section revealing fluorescent granules in the RPE (bottom). (**c**) Images of the RPE in a live albino 7-week-old $Rpe65^{-/-}$ mouse obtained with 730-nm and 850-nm excitation. (**d**) Fluorescence emission spectra from RPE of 7-week-old $Abca4^{-/-}$; $Rdh8^{-/-}$ mice obtained with 850 nm and 7-week-old $Rpe65^{-/-}$ mice obtained with 730-nm excitation light *in vivo*. (**e**) Quantification of fluorescent granules. Error bars indicate mean ± s.d., $n = 3$ eyes per group. Scale bars, 60 μm (**b** and **c**).

the RPE of *Rpe65^{−/−}* mice with 730-nm excitation, which revealed maxima at 480 nm and 511 nm and a shoulder at 463 nm, whereas the spectrum we obtained from DKO mice with 850-nm excitation was shifted to longer wavelengths (**Fig. 4d**). The emission maxima at both 480 nm and 511 nm are probably generated by retinyl esters[5,31], whereas the shoulder at 463 nm is probably generated by NADPH[32]. The maximum around 511 nm could also be derived from all-*trans*-retinal[33], but the abundance of retinyl esters in *Rpe65^{−/−}* mice favors these retinoids as the primary source.

We counted on average 536 fluorescent granules per mm^2 (**Fig. 4e**). The difference in the number of granules found with *ex vivo* (**Fig. 3d**) versus *in vivo* (**Fig. 4e**) imaging was not statistically significant. The uneven edges of the cornea and lens sutures (**Fig. 4b**), corresponding to ~145 breaths per minute of the mouse, resulted from using a slower acquisition rate for this image. Examination of TPM RPE images obtained during DM surface optimization did not indicate damage to RPE (**Supplementary Video 2**).

DISCUSSION

This work offers several advances over previous reports of TPM imaging of the retina[3,5,7,10]. These include, to our knowledge, (i) the first images of retinoid cycle fluorophores in the RPE of living pigmented mammals and their spectral and spatial characterization; (ii) the first TPM images of rod photoreceptor cells; and (iii) the characterization of endogenous and artificial fluorophores in retinas affected by genetic disorders, environmental stress or drug therapy.

As TPM technology improves, we can expect high-resolution images without jeopardizing safety, which will facilitate its translation into clinical applications. When imaging pigmented animals, more noise will occur because of a relatively uniform distribution of melanin within the RPE and microvilli. However, melanin fluorescence in response to infrared light has been reported to be 60 to 100 times less than the fluorescence of lipofuscin[34]. This finding, combined with our results in pigmented animals, makes us optimistic about prospects of using TPM to image the human eye.

TPM can be used to accelerate drug discovery and development by rapidly evaluating how compounds interact with tissues by determining their *in vivo* sites of action, as well as treatment safety and efficacy. Together with insights derived from parallel molecular, cellular and pathophysiological studies, TPM can foster effective treatment strategies for retinal diseases such as AMD, Stargardt's disease and diabetic retinopathy. The cost effectiveness of using software-driven adaptive optics will make TPM an attractive tool as therapeutic research transitions from mice to humans.

Applications of nonendogenous fluorescent proteins will allow monitoring of protein expression, translocation and changes in specific cell types expressing customized protein fluorescent sensors. Such fluorophores could provide clues about ensuing pathology for common central nervous system diseases such as multiple sclerosis and Alzheimer's disease[35]. 2PE-based imaging of the eye can potentially be used to understand the connectivity and function of retinal neurons *in vivo*, including pathological changes such as neovascularization within the retina or brain damage after a stroke.

The applications of multiphoton excitation complement yet far exceed the capabilities of either optical coherence tomography[36] or scanning laser ophthalmoscopy[37]. Optical coherence tomography cannot visualize fluorophores. TPM can image fluorophores that are accessible to scanning laser ophthalmoscopy only when using retina-harming ultraviolet light[38]. Additionally, the longer excitation wavelengths employed by TPM are less prone to scattering when traveling through the tissue. Specifically, TPM can detect vitamin A metabolites and their toxic byproducts, thus making it the best current method to nondestructively monitor disease progression in the same animal.

There is minimal information available regarding retinal damage in mice from laser pulses of less than 100-fs duration. However, considering that it took 4–6 min to achieve an optimal DM shape, as well as in light of previous reports[39], our laser power was almost ten times higher than safety limits based on thermal continuous-wave calculations for multiple exposures[38]. Nonetheless, we did not detect any damage after TPM imaging. Improved detectors and further shortened laser pulses will reduce the laser power required to obtain retinal images[40]. However, extensive safety studies in mice and primates are needed before this technology is employed in humans.

METHODS

Methods and any associated references are available in the online version of the paper.

1. Helmchen, F. & Denk, W. Deep tissue two-photon microscopy. *Nat. Methods* **2**, 932–940 (2005).
2. Boettner, E.A. & Wolter, J.R. Transmission of the ocular media. *Invest. Ophthalmol. Vis. Sci.* **1**, 776–783 (1962).
3. Imanishi, Y., Batten, M.L., Piston, D.W., Baehr, W. & Palczewski, K. Noninvasive two-photon imaging reveals retinyl ester storage structures in the eye. *J. Cell Biol.* **164**, 373–383 (2004).
4. Imanishi, Y., Gerke, V. & Palczewski, K. Retinosomes: new insights into intracellular managing of hydrophobic substances in lipid bodies. *J. Cell Biol.* **166**, 447–453 (2004).
5. Palczewska, G. *et al.* Noninvasive multiphoton fluorescence microscopy resolves retinol and retinal condensation products in mouse eyes. *Nat. Med.* **16**, 1444–1449 (2010).
6. Denk, W., Strickler, J.H. & Webb, W.W. Two-photon laser scanning fluorescence microscopy. *Science* **248**, 73–76 (1990).
7. Hunter, J.J. *et al.* Images of photoreceptors in living primate eyes using adaptive optics two-photon ophthalmoscopy. *Biomed. Opt. Express* **2**, 139–148 (2010).
8. Godara, P., Dubis, A.M., Roorda, A., Duncan, J.L. & Carroll, J. Adaptive optics retinal imaging: emerging clinical applications. *Optom. Vis. Sci.* **87**, 930–941 (2010).
9. Liang, J., Williams, D.R. & Miller, D.T. Supernormal vision and high-resolution retinal imaging through adaptive optics. *J. Opt. Soc. Am. A Opt. Image Sci. Vis.* **14**, 2884–2892 (1997).
10. Sharma, R. *et al. In vivo* two-photon imaging of the mouse retina. *Biomed. Opt. Express* **4**, 1285–1293 (2013).
11. Rueckel, M., Mack-Bucher, J.A. & Denk, W. Adaptive wavefront correction in two-photon microscopy using coherence-gated wavefront sensing. *Proc. Natl. Acad. Sci. USA* **103**, 17137–17142 (2006).

12. Huang, S., Heikal, A.A. & Webb, W.W. Two-photon fluorescence spectroscopy and microscopy of NAD(P)H and flavoprotein. *Biophys. J.* **82**, 2811–2825 (2002).

13. Padayatti, P., Palczewska, G., Sun, W., Palczewski, K. & Salom, D. Imaging of protein crystals with two-photon microscopy. *Biochemistry* **51**, 1625–1637 (2012).

14. Kiser, P.D., Golczak, M., Maeda, A. & Palczewski, K. Key enzymes of the retinoid (visual) cycle in vertebrate retina. *Biochim. Biophys. Acta* **1821**, 137–151 (2012).

15. Palczewski, K. Chemistry and biology of vision. *J. Biol. Chem.* **287**, 1612–1619 (2012).

16. von Lintig, J., Kiser, P.D., Golczak, M. & Palczewski, K. The biochemical and structural basis for *trans*-to-*cis* isomerization of retinoids in the chemistry of vision. *Trends Biochem. Sci.* **35**, 400–410 (2010).

17. Sparrow, J.R., Wu, Y., Kim, C.Y. & Zhou, J. Phospholipid meets all-*trans*-retinal: the making of RPE bisretinoids. *J. Lipid Res.* **51**, 247–261 (2010).

18. Maeda, A. *et al.* Primary amines protect against retinal degeneration in mouse models of retinopathies. *Nat. Chem. Biol.* **8**, 170–178 (2011).

19. Maeda, T. *et al.* QLT091001, a 9-*cis*-retinal analog, is well-tolerated by retinas of mice with impaired visual cycles. *Invest. Ophthalmol. Vis. Sci.* **54**, 455–466 (2013).

20. Golczak, M., Kuksa, V., Maeda, T., Moise, A.R. & Palczewski, K. Positively charged retinoids are potent and selective inhibitors of the *trans-cis* isomerization in the retinoid (visual) cycle. *Proc. Natl. Acad. Sci. USA* **102**, 8162–8167 (2005).

21. Lin, B., Wang, S.W. & Masland, R.H. Retinal ganglion cell type, size, and spacing can be specified independent of homotypic dendritic contacts. *Neuron* **43**, 475–485 (2004).

22. Euler, T. *et al.* Eyecup scope—optical recordings of light stimulus-evoked fluorescence signals in the retina. *Pflugers Arch.* **457**, 1393–1414 (2009).

23. Bueno, J.M., Gualda, E.J. & Artal, P. Adaptive optics multiphoton microscopy to study *ex vivo* ocular tissues. *J. Biomed. Opt.* **15**, 066004 (2010).

24. Helmstaedter, M. *et al.* Connectomic reconstruction of the inner plexiform layer in the mouse retina. *Nature* **500**, 168–174 (2013).

25. Sun, W., Li, N. & He, S. Large-scale morphological survey of mouse retinal ganglion cells. *J. Comp. Neurol.* **451**, 115–126 (2002).

26. Zipfel, W.R., Williams, R.M. & Webb, W.W. Nonlinear magic: multiphoton microscopy in the biosciences. *Nat. Biotechnol.* **21**, 1369–1377 (2003).

27. Chan, F., Bradley, A., Wensel, T.G. & Wilson, J.H. Knock-in human rhodopsin-GFP fusions as mouse models for human disease and targets for gene therapy. *Proc. Natl. Acad. Sci. USA* **101**, 9109–9114 (2004).

28. Spiess, E. *et al.* Two-photon excitation and emission spectra of the green fluorescent protein variants ECFP, EGFP and EYFP. *J. Microsc.* **217**, 200–204 (2005).

29. Schmucker, C. & Schaeffel, F. A paraxial schematic eye model for the growing C57BL/6 mouse. *Vision Res.* **44**, 1857–1867 (2004).

30. Katz, M.L. & Redmond, T.M. Effect of Rpe65 knockout on accumulation of lipofuscin fluorophores in the retinal pigment epithelium. *Invest. Ophthalmol. Vis. Sci.* **42**, 3023–3030 (2001).

31. Drabent, R., Bryl, K., Smyk, B. & Ulbrych, K. Retinyl palmitate in water environment. *J. Photochem. Photobiol. B* **37**, 254–260 (1997).

32. Chen, C. *et al.* Reduction of all-*trans* retinal to all-*trans* retinol in the outer segments of frog and mouse rod photoreceptors. *Biophys. J.* **88**, 2278–2287 (2005).

33. Moroni, L., Gellini, C., Salvi, P.R. & Schettino, V. Fluorescence of all-*trans*-retinal as a crystal and in a dense solution phase. *J. Phys. Chem. A* **104**, 11063–11069 (2000).

34. Keilhauer, C.N. & Delori, F.C. Near-infrared autofluorescence imaging of the fundus: visualization of ocular melanin. *Invest. Ophthalmol. Vis. Sci.* **47**, 3556–3564 (2006).

35. London, A., Benhar, I. & Schwartz, M. The retina as a window to the brain-from eye research to CNS disorders. *Nat. Rev. Neurol.* **9**, 44–53 (2013).

36. Kocaoglu, O.P. *et al.* Imaging cone photoreceptors in three dimensions and in time using ultrahigh resolution optical coherence tomography with adaptive optics. *Biomed. Opt. Express* **2**, 748–763 (2011).

37. Carroll, J. *et al.* The effect of cone opsin mutations on retinal structure and the integrity of the photoreceptor mosaic. *Invest. Ophthalmol. Vis. Sci.* **53**, 8006–8015 (2012).

38. Delori, F.C., Webb, R.H., Sliney, D.H. & American National Standards, I. Maximum permissible exposures for ocular safety (ANSI 2000), with emphasis on ophthalmic devices. *J. Opt. Soc. Am. A Opt. Image Sci. Vis.* **24**, 1250–1265 (2007).

39. Geng, Y. *et al.* Adaptive optics retinal imaging in the living mouse eye. *Biomed. Opt. Express* **3**, 715–734 (2012).

40. Xi, P., Andegeko, Y., Pestov, D., Lovozoy, V.V. & Dantus, M. Two-photon imaging using adaptive phase compensated ultrashort laser pulses. *J. Biomed. Opt.* **14**, 014002 (2009).

ONLINE METHODS

Mice. All animal procedures and experiments were approved by the Institutional Animal Care and Use Committee at Case Western Reserve University and conformed to recommendations of both the American Veterinary Medical Association Panel on Euthanasia and the Association for Research in Vision and Ophthalmology. B6(Cg)-Tyr^{c-2J}/J mice were purchased from The Jackson Laboratory. $Abca4^{-/-}$; $Rdh8^{-/-}$ (DKO) and $Rpe65^{-/-}$ mice were generated and genotyped as previously described[5]. Human rhodopsin–GFP fusion, knock-in Rho^{tm2Jhw} mice, sometimes referred to as $hrhoG/hrhoG$ mice, expressing human rhodopsin–GFP in photoreceptor outer segments, were provided by J. Wilson (Baylor College of Medicine)[27]. All mice were housed in the animal facility at the School of Medicine, Case Western Reserve University, where they were provided with a regular mouse chow diet and maintained either under complete darkness or in a 12-h light (~10 lx)–12-h dark cyclic environment. Euthanasia was performed in compliance with American Veterinary Medical Association (AVMA) Guidelines on Euthanasia and approval by the Case Western Reserve University Institutional Animal Care and Use Committee. All mice used in this study were between 1 and 6 months old. We used both male and female animals.

DKO mouse pupils were dilated with 1% tropicamide before bright white light exposure at 10,000 lx (150 W spiral lamp, Commercial Electric) for 60 min. After bright light exposure, animals were housed in the dark until subsequent imaging sessions. Two-photon imaging to assess RPE and retinal changes was performed 7 and 14 d after bright light exposure.

Two-photon imaging was done through mouse eye pupil unless otherwise indicated, either *in vivo* or *ex vivo* with freshly enucleated mouse eyes. For *in vivo* imaging, mice were anesthetized with an intraperitoneal injection of anesthetic solution consisting of ketamine (15 mg/ml), xylazine (3 mg/ml) and acepromazine 0.5 mg/ml diluted with water at a dose of 10 μl/g body weight (bw).

To enhance the visibility of retinosomes, WT mice without any drug treatment or treated with Ret-NH$_2$ were exposed to 5,000 lx of white light for 5–30 min, 1 to 3 h before imaging.

Optical coherence tomography. Optical coherence tomography (OCT) imaging to verify retina integrity after TPM imaging was performed using SD-OCT Envisu R2200 (Bioptigen, Morrisville, NC).

Retinylamine treatment. Ret-NH$_2$ was synthesized as described previously[20]. Mice (4 to 6 weeks old) were gavaged with 2 mg of Ret-NH$_2$ solubilized in 100 μl soybean oil 13 to 16 h before bright light exposure. Two-photon imaging was performed 7 and 14 d after bright light exposure.

After treatment with Ret-NH$_2$, the content of fluorescent retinyl esters increases in the eye as reported previously[20,41]. However, 7 d after treatment, that increase diminishes[42]. For quantification of the impact of drug treatment, the same detector settings were used for mice that were treated and not treated with Ret-NH$_2$. This also applied to imaging with either 730 nm or 850 nm excitation. To prevent overload of the detector in this experiment, the settings were optimized to visualize condensation products (not retinyl esters), which were abundant in animals that were not treated with Ret-NH$_2$. This is why outlines of RPE cell borders are only very slightly visible in animals that were treated with Ret-NH$_2$.

The fluorescence intensity was brighter 14 d after light exposure than 7 d after exposure because it took some time for RPE cells to accumulate condensation products resulting from light exposure in mice that were not treated with Ret-NH$_2$.

Two-photon imaging system for mouse retina and retinal pigment epithelium. To achieve 2PE images of the retina and RPE with laser light entering through the mouse eye pupil, we modified the Leica (Wetzlar, Germany) TCS SP5 to include the following: an upright DM600 microscope stand, a Chameleon Vision–S (Coherent, Santa Clara, CA) femtosecond laser, an objective with a 0.5 numerical aperture and 15 mm working distance and a custom adaptive optics system including a deformable mirror (DM) (**Fig. 1a,b**).

The tunable, 690–1050 nm, Chameleon Vision-S generated 75 fs laser pulses at 80 MHz pulse repetition frequency. To minimize laser pulse duration

at the sample, the laser was equipped with a group velocity dispersion precompensation (DC) unit with a 0 to 43,000 fs^2 range. Laser beam power was controlled with an electro–optic modulator (EOM) contained within a safety box. After the EOM, the laser beam was directed to the adaptive optics component, namely DM, by the fold mirror on a kinematic magnetic base (FMK1). The laser beam was coupled to the DM with expander lenses L1 and L2 (**Fig. 1c**). A micro-electro-mechanical system DM (Boston Micromachines Corp., Cambridge, MA) with 140 actuators, a 5.5 μm stroke and gold coating provided fine focus adjustment and correction of aberrations introduced by the sample. In two-photon imaging, the excitation matters most because the emission fluorescence is generated only in the focal spot; therefore, it is critical to achieve a tightly focused excitation beam. Only the excitation light was modulated by the DM, whose shape was controlled with software based on image quality metric feedback without the use of a wavefront sensor and associated components[7,39,43]. This design reduced the cost of the system and its footprint. Lenses L3 and L4 reduced the size of the beam which, after reflecting off the second fold mirror on a kinematic magnetic base (FMK2), was directed to the scan mirrors. The scan mirrors, which operated with typical line frequency of 400 to 700 Hz with 512 to 1,024 lines per frame and typical pixel dwell time of 1.46 μs, were located at the plane conjugate to the back aperture of the 0.5 numerical aperture (NA) objective. In this configuration, the laser beam overfilled the mouse eye to take advantage of the NA of the dilated pupil. Laser power entering the pupil was 7.4 mW, based on an estimated 3.2-mm laser beam diameter and a 2-mm mouse eye pupil. We verified that estimate by placing a 2 mm iris at a location corresponding to the mouse eye pupil and measuring 8.5 mW using a laser power meter. Additionally, we measured that the needed laser light levels could be cut by over 25%. Only 6.3 mW of laser power was needed for imaging with this HYD detector, as compared to 8.5 mW of laser power required to obtain TPM images with the photomultiplier tube (PMT) detector. This represents an over 25% reduction in required laser power. This reduction is consistent with the HYD detector's higher quantum yield. At 500 nm, the quantum yield of the HYD detector was ~45% as compared to the 27% quantum yield of the PMT R6357 detector used throughout the study, (**Supplementary Fig. 3**). The fluorescence detector was located as close to the sample as possible to minimize loss of light available for image formation. Two-photon excited fluorescence leaving mouse eye pupil was collected by the same 0.5 NA lens and directed to the PMT detector, Hamamatsu R6357, in a nondescanned manner after the excitation light was reflected off the dichroic mirror (DCh) and filtered by the 680SPET Leica filter. 2PE spectra were obtained with a spectrally sensitive detector in a descanned configuration. For *ex vivo* imaging, the mouse eye was submerged in PBS composed of 9.5 mM sodium phosphate, 137 mM NaCl and 2.7 mM KCl, pH 7.4, with the pupil facing the excitation laser beam. For *in vivo* mouse imaging, the animal was surrounded by a heating pad and placed on a mechanical stage, which provided controlled movement around two rotational and in three translational axes (Bioptigen, Morrisville, NC). The mouse eye was covered with GenTeal gel that provided lubrication and refractive index-matching with the RGP hard contact lens with a refractive index of 1.46, a radius of 1.7 mm and a flat front surface (Cantor and Nissel, Northamptonshire, UK). This contact lens directed laser light into the mouse eye, compensated for the refractive power of the cornea-air interface, minimized the impact of corneal deformities and protected cornea from drying during the imaging session.

No changes to the cornea and lens were detectable using a low magnification sectioning microscope after completion of the imaging. Additionally, four weeks after TPM imaging of $Rpe65^{-/-}$ mice, we used OCT to check the integrity of retinal layers. No differences were noted between mice that were imaged with TPM and control age-matched $Rpe65^{-/-}$ mice that were not imaged. Specifically, the outer nuclear layer average thickness in mice imaged with TPM was equal to 0.040 mm, with s.d. of 0.002 mm, whereas corresponding measurements in control mice that were not imaged with TPM were 0.037 mm with s.d. of 0.004 mm (**Supplementary Fig. 4**).

The scale bars displayed in the images were estimated by comparing measurements of *en face* TPM images of optic disks and histological sections.

LAS AF Leica software and raw image data were used for quantification of fluorescent granules and fluorescence. Granules were counted in the inferior/central portion of the retina. The area selected was about 100 μm away from

the edge of the optic disc. The RPE sampling area was kept between 0.05 mm^2 and 0.1 mm^2 for each eye. An example of the distribution of fluorescent granules around the optic disc is shown in **Figure 3e**.

To calculate resolution along the optical axis (z axis) as described in results referring to **Figure 2d**, we used 730 nm excitation, with the numerical aperture (NA) of the mouse eye equal to 0.4 and the coefficient of refraction of the vitreous humor equal to 1.33 (ref. 44).

Image acquisition algorithm. After focusing on the mouse RPE with a mechanical stage, optimization of the DM surface provided fine adjustments of focus and the excitation wavefront. Six Zernike modes were used as the set of basis functions for deformation of the DM surface. Zernike modes are a set of polynomials that are orthogonal to one another and frequently used to describe ophthalmic aberrations[45]. The six modes used were $Z_2^0, Z_2^2, Z_2^{-2}, Z_3^1, Z_3^{-1}, Z_4^0$ (ref. 45). The aberration compensation, Φ, provided by the DM was $\Phi = \Sigma\alpha_j Z_j$, where Z_j is the Zernike mode with index j and the coefficient α_j is the contribution of Z_j. The coefficients were constrained such that $-1.0 < \alpha_j < 1.0$. The goal of optimizing the DM surface was to find a set of α coefficients which maximize the quality metric of a collected image. The quality metric used here was the normalized variance of the image[46].

Optimization was performed by one of two procedures. In the first, the six Zernike modes were sequentially optimized. Starting with focus, Z_2^0, the coefficient α_1 was varied from −0.9 to 0.72 in steps of 0.18, and the normalized variance was calculated at each step. The α_1 of the step that provided the best normalized variance value for the collected image was taken as the optimized coefficient for Z_2^0. The $\alpha_1 Z_2^0$ was applied to the initially flat DM surface, and the procedure was repeated for the other aberration terms ($Z_2^2, Z_2^{-2}, Z_3^1, Z_3^{-1}, Z_4^0$) such that the optimized Zernike modes accumulated on the DM surface. In the end, the vector of α_j had been determined, and the mirror had accumulated the corresponding surface shape. This procedure was applied to image the *Rho^{tm2Jhw}* mice. The set of such established coefficients was 0.72, −0.18, 0.00, 0.00, 0.18 and 0.00 for Zernike modes as listed above. The normalized variance of the image taken with these coefficients was 1,717 versus the image collected with a flat mirror, which had a normalized variance value of 246. This process collected 60 images and took 4–6 min to complete. However, the image with the best normalized variance value was not the image collected with the coefficients determined by the end of the process. The individual rod cells in *Rho^{tm2Jhw}* mice are difficult to distinguish initially without DM correction because of their small features. Sequential optimization was used to image *Rho^{tm2Jhw}* mice because each step is more independent of the previous one than in the second method described below. During sequential optimization, there is dependence on the previous steps because each subsequent Zernike mode builds off of the previous optimized Zernike mode. However, in the worst case, this would still provide at minimum ten images with varying coefficients for defocus from which to choose. Here, the image with the best normalized variance (**Fig. 3b**) was collected during the defocus optimization stage, providing coefficients of −0.72, 0.00, 0.00, 0.00, 0.00 and 0.00 and a normalized variance value of 1,943. One possible reason why the image resulting from the complete sequential optimization was not the best in this case could be the influence of changes in the mouse eye itself, as this optimization was performed on a euthanized mouse. The second procedure for DM optimization is based on the stochastic parallel gradient descent (SPGD) method previously described[47]. The normalized variance value, V, was calculated for an image

collected using an initial set of α coefficients, specifically, all $\alpha_j = 0$, which corresponds to a flat DM. Next, all α_j were perturbed by a small amount, ζ_j, randomly chosen from between −0.05 and 0.05 in steps of 0.025, but excluding 0.0. This provided a new set of coefficients, $\alpha_j + \zeta_j$. Using the new coefficients, a second image was collected, and the normalized variance was calculated to get V_ζ. Starting coefficients for the next iteration (i) were then calculated as $\alpha_j^{i+1} = \alpha_j - \eta\zeta_j(V_\zeta - V)$, where η is the learning rate. Here a value of −0.01 was used for η, which is negative because the normalized variance was being maximized. The iterative process was performed for 40 steps, and the DM surface that provided the largest normalized variance value was taken as optimal. This procedure was used to image live *Rpe65^{−/−}* mice (images shown in **Fig. 4c**). The optimization improved the normalized variance of 2,374 for a flat DM to a value of 3,024 for an optimized DM surface. The optimized coefficients for this mouse were −0.48, 0.05, 0.28, −0.08, −0.06 and −0.24.

The sequential and SPGD optimization methods offer complementary approaches for improving image quality. The sequential optimization performs a search over a broad range of Zernike mode coefficients, which is useful if there are large aberrations. If the features of interest are not resolved initially after sample preparation, the gradients needed by SPGD may be difficult to determine, but sequential optimization will systematically search and find coefficients that improve image quality. However, for sequential optimization, the search is coarse, and the coefficients are not simultaneously optimized, in order to allow broad sampling within a reasonable time frame. The SPGD performs gradient based optimization simultaneously for all Zernike modes. If the desired features can be resolved after initially localizing and focusing the sample, SPGD could more precisely determine the optimal coefficients compared to sequential optimization. However, SPGD requires the collection of more images and therefore requires more time than sequential optimization. Therefore, based on the preparation and initial setup of the sample, one can decide whether SPGD or sequential optimization will be more appropriate, as eyes and aberrations differ greatly even within mice of the same genetic makeup.

Statistical analyses. Data in the bar graphs are expressed as the mean ± s.d. The statistical analyses were carried out with analysis of variance. Differences with P values > 0.05 were considered not statistically significant.

41. Golczak, M. *et al.* Lecithin:retinol acyltransferase is responsible for amidation of retinylamine, a potent inhibitor of the retinoid cycle. *J. Biol. Chem.* **280**, 42263–42273 (2005).
42. Maeda, A. *et al.* Effects of potent inhibitors of the retinoid cycle on visual function and photoreceptor protection from light damage in mice. *Mol. Pharmacol.* **70**, 1220–1229 (2006).
43. Zhang, Y., Poonja, S. & Roorda, A. MEMS-based adaptive optics scanning laser ophthalmoscopy. *Opt. Lett.* **31**, 1268–1270 (2006).
44. Remtulla, S. & Hallett, P.E. A schematic eye for the mouse, and comparisons with the rat. *Vision Res.* **25**, 21–31 (1985).
45. Thibos, L.N. *et al.* Standards for reporting the optical aberrations of eyes. *J. Refract. Surg.* **18**, S652–S660 (2002).
46. Sun, Y., Duthaler, S. & Nelson, B.J. Autofocusing in computer microscopy: selecting the optimal focus algorithm. *Microsc. Res. Tech.* **65**, 139–149 (2004).
47. Vorontsov, M.A. & Sivokon, V.P. Stochastic parallel-gradient-descent technique for high-resolution wave-front phase-distortion correction. *J. Opt. Soc. Am. A Opt. Image Sci. Vis.* **15**, 2745–2758 (1998).